JOURNAL OF GUIDANCE, CONTROL, AND DYNAMICS
Vol. 31, No. 6, November–December 2008

Mars Aerobraking Spacecraft State Estimation by Processing Inertial Measurement Unit Data

Moriba K. Jah*
U.S. Air Force Research Laboratory, Kihei, Hawaii 96753
Michael E. Lisano II†
Jet Propulsion Laboratory,
California Institute of Technology, Pasadena, California 91040
and
George H. Born‡ and Penina Axelrad§
University of Colorado, Boulder, Colorado 80309

DOI: 10.2514/1.24304

Aerobraking is an efficient technique for orbit adjustment of planetary spacecraft, such as the Magellan (Venus), the Mars Global Surveyor, and the Mars Odyssey. Determination of the vehicle state during the aerobraking phase has conventionally been performed using only radiometric tracking data before and following the atmospheric drag pass. This approach is sufficiently accurate and timely to meet current mission operational requirements; however, it is human-hour-intensive and leads to delayed results because of the need for post-drag-pass data. This research presents a new approach to estimation of the vehicle state during the atmospheric pass that sequentially incorporates observations from an inertial measurement unit and models of the vehicle and environment. The approach, called inertial measurements for aeroassisted navigation, has a comparable navigation accuracy and superior availability of the results immediately after completion of the pass against current navigation team solutions. Furthermore, the research shows that inertial measurements for aeroassisted navigation can be used to reliably predict subsequent periapsis times and locations over all aerobraking regimes; it also yields accurate peak dynamic pressure and heating rates, critical for a successful corridor control strategy. This research also provides the first instance of the utilization of the unscented Kalman filter for the purpose of estimating an actual spacecraft trajectory arc about another planet.

I. Introduction

AEROBRAKING is a spaceflight technique that makes use of atmospheric drag to decrease the velocity of a spacecraft. It is a method that has been successfully implemented by the Magellan (at Venus), the Mars Global Surveyor, the Mars Odyssey, and the Mars Reconnaissance Orbiter. This is coupled with a proportional decrease in the semimajor axis of the orbit. Initially, the vehicle is inserted into a highly eccentric orbit with periapse located within the atmospheric influence of the planet. The spacecraft employing aerobraking is designed to traverse a specific atmospheric corridor, historically based upon heat rate or dynamic pressure. Aerobraking is employed until the desired apoapse altitude is achieved, at which time the spacecraft performs a propulsive periapse-raising maneuver, placing it in its final orbital configuration. The use of aerobraking for orbit adjustment reduces the required propellant and, consequently, both the spacecraft mass and mission cost.

Aerobraking introduces operational costs and risks; examples from flown missions to date include the following:

1) The spacecraft slews into a designed aerodynamically-stable orientation before each drag pass. Traditionally, there is a loss of radiometric tracking when the spacecraft is in this most dynamically unknown portion of its trajectory. This is due to conflicts between physical constraints in spacecraft design (such as possible articulation or fixed placement of antennas) and variable spacecraft-to-Earth geometry throughout aerobraking required for tracking. Because of the lack of tracking data, this results in a significant increase of the post-drag-pass spacecraft state (i.e., position and velocity) uncertainty.

2) The aerobraking orbit reconstruction process can be very time-consuming (several hours for each orbit) and workforce-intensive (six full-time-equivalent navigators for the 3-month Mars Odyssey 24/7 aerobraking operations). In contrast, nominal navigation operations consist of a traditional work week and workforce (two or three navigators working 8-h days, 5 days a week).

3) All of the spacecraft events occur on a ground-generated time line, via a sequence of commands, that is uploaded to the spacecraft and is triggered by the onboard clock. In order for this sequence to be produced, the navigation team must receive post-drag-pass radiometric data and deliver a predicted trajectory. Any delay in receiving this may compromise spacecraft safety as an updated sequence may not be generated for the subsequent pass. The spacecraft would then have to rely on a less accurate background sequence.

4) Spacecraft events take place at times relative to the predicted time of periapse. Significant errors in this prediction (greater than 225 s) could lead to

a) Aerobraking corridor control maneuver errors and, thus, inefficient propellant usage.

b) Spacecraft attitude errors exceeding a 20-deg bandwidth at the time of control authority switch from reaction wheels to attitude control thruster system, capable of inducing inadvertent compensative thruster firings, and, thus, another source of inefficient propellant usage. Inadvertent safe-mode entry triggering is another possible outcome.

Presented as Paper 5920 at the SpaceOps 2006 Conference, Rome, 19–23 June 2006; received 28 March 2006; accepted for publication 12 December 2007. Copyright © 2008 by the American Institute of Aeronautics and Astronautics, Inc. The U.S. Government has a royalty-free license to exercise all rights under the copyright claimed herein for Governmental purposes. All other rights are reserved by the copyright owner. Copies of this paper may be made for personal or internal use, on condition that the copier pay the $10.00 per-copy fee to the Copyright Clearance Center, Inc., 222 Rosewood Drive, Danvers, MA 01923; include the code 0731-5090/08 $10.00 in correspondence with the CCC.

*Senior Research Astrodynamicist, Air Force Maui Optical and Supercomputing Site, 535 Lipoa Parkway Suite 200.

†Senior Engineering Staff, Guidance Navigation and Control Section, 4800 Oak Grove Drive.

‡Director and Professor, Colorado Center for Astrodynamics Research, Aerospace Engineering Sciences, Campus Box 41, Boulder, CO 80301.

§Professor and Associate Chair, Colorado Center for Astrodynamics Research, Aerospace Engineering Sciences, Campus Box 41.

These costs and risks can be mitigated by making use of the information provided by inertial measurement units (IMU) for navigation, augmenting current navigation capabilities, and providing mission robustness. The IMU gyroscopes provide data on the rotational states of the spacecraft, whereas the accelerometers measure the effects of nongravitational forces, such as those due to atmospheric drag. This project demonstrates how to exploit this sensitivity for navigation performance, and, thus, reduce cost and risk.

Historical uses of IMUs for interplanetary spacecraft are deterministic (i.e., used in lieu of a dynamic model), and, as a result, do not statistically improve the knowledge of the spacecraft state. This research implements the IMU data as orbit-determination measurements, providing post-drag-pass spacecraft position and velocity estimates, realistic reconstructed atmospheric density profiles, and accurate subsequent periapsis time estimates, without the need to process post-drag-pass radiometric data; it is an independent assessment of the drag-pass dynamics. The information provided by an IMU is strongly dependent on the initial conditions, because the IMU measurements are relative to the initial state of the spacecraft.

The IMU-based spacecraft state estimates are achieved more rapidly than those achieved historically, which require the collection and reduction of post-drag-pass radiometric data. Because Mars-bound spacecraft are already equipped with IMUs, making use of these measurements comes at no additional hardware expense to a flight project.

The ultimate goal of this research is to pave a road for future aerobraking missions, leading to the capability of onboard navigation. This ability would allow for the spacecraft to autonomously perform aerobraking corridor control maneuvers and drag-pass/Earth communication attitude slews, breaking away from current ground operations dependency. To validate the approach of using the IMU data type for aerobraking navigation, two research routes were taken; the first was to process simulated IMU data, and the second was to process flight IMU data.

A. Historical Uses of IMU Data and Previous Research

The use of IMU data as orbit-determination measurements [1,2] was suggested as early as 30 years ago [3]. However, the use of IMU data in this capacity was not implemented for various reasons. One main reason was that until recently, these instruments were too massive and power-intensive to be included as a standard spacecraft payload. Current technology, such as multisensor inertial measurement units (MIMU), allows IMUs to be standard spacecraft payloads, making use of these data for navigation monetarily transparent to any mission.

Typical uses for accelerometer data on interplanetary missions have been used to control and assess propulsive maneuvers, orbit insertions, and atmospheric entries. Interplanetary maneuvers are either sequenced or autonomous. They are not commanded in real time due to radio signal light-time travel constraints. IMUs are also used as thruster cutoff sensors by measuring the amount of applied thrust and triggering the shutoff upon reaching the designed thrust levels. Typically, there is a redundant shutoff system based upon a thruster-on timer, and, should the IMU fail, the thruster will shut off once the allotted time has expired. This shutoff procedure is also applied for trajectory correction maneuvers and aerobraking maneuvers (ABMs).

Earth-based missions, such as GRACE, use the accelerometer data as a means of measuring nongravitational accelerations in order to refine knowledge of the gravitational field of the Earth. IMU data collected during space shuttle operations have been used to characterize the rarefied flow regime encountered during reentry and to formulate realistic aerodynamic coefficient tables [4].

During planetary entry descent landing (EDL), the IMU output is used onboard in lieu of nongravitational dynamic equations. This has been the case for both the Viking and Mars Pathfinder missions. There has been recent work in this area (EDL) seeking to incorporate IMU data as navigation measurements instead of the traditional use of the data directly into the computed dynamics, [5,6].[¶] For aerobraking, the IMU data has been used as a deterministic drag-pass assessment tool. Willcockson and Johnson [7] developed a periapse timing estimator (PTE), which takes the IMU data as truth and returns an estimate of the drag-pass change in velocity along with the time at which the centroid of the drag pass occurred. It uses this information to predict the subsequent periapsis time, based on an analytic equation relating change in velocity to change in orbit period. This method does not filter the IMU data, nor does it integrate a trajectory. Rather, it compares several drag-pass metrics with those predicted by the navigation team and suggests corrections.

B. Overview of Research

Section II provides an overview of the navigation strategies common to the aerobraking phase of a mission. Pros and cons are presented along with current aerobraking navigation accuracy capabilities. Section III provides information relating to the typical sources of error associated with the IMU measurements used. The section also formulates the IMU measurement model. Section IV specifically describes the inertial measurements for aeroassited navigation tool designed and developed in this research. Section V provides results from processing flight data obtained from the 2001 Mars Odyssey orbiter mission. Finally, Sec. VI provides a summary of this research, the conclusions, and makes recommendations for the direction of future work in this area.

II. Aerobraking Operations and Strategies

A. Current Procedure and Methodology

To date, there have been four successful interplanetary aerobraking missions: the Magellan at Venus [8,9], the Mars Global Surveyor [10], the Mars Odyssey [11], and the Mars Reconnaissance Orbiter. The spacecraft employing aerobraking is set to traverse a designed atmospheric corridor. For Mars Odyssey, the performance index of choice is heat rate (in units of W/cm^2), which is defined by comparing [12] in Eq. (1). Alternatively, for the Mars Global Surveyor and the Magellan, this performance index was atmospheric dynamic pressure

$$\dot{q} = \tfrac{1}{2}\rho V^3 \tag{1}$$

where $\dot{q}$ is the heat rate, ρ is the local density, and V is the inertial velocity of the spacecraft relative to the atmosphere.

The spacecraft can only tolerate a finite amount of heat for a given amount of time, making the heat rate a required corridor control parameter. The heat rate and maximum temperature set the upper limit of the aerobraking corridor. There is usually a mapping orbit constraint driving the maximum duration that can be spent aerobraking; the lower limit is set such that the spacecraft can survive for a given amount of time without an orbit adjustment. For Mars Odyssey, this amount of time was 48 h.

The spacecraft velocity is greatest at periapse. Thus, predicting the periapse altitude is directly related to the ability in predicting the spacecraft velocity magnitude at periapse. Because one of the parameters that the heat rate is a function of is the spacecraft velocity, being able to predict this velocity is important. The main perturbing factor influencing periapse altitude is the gravitational field. Therefore, modeling the gravity accurately is critical in order to minimize spacecraft state errors. When a high-density value is estimated following the drag pass, what must be successfully determined is whether the increase in density occurred due to a lower periapse altitude or an expanding atmosphere (e.g., dust storm). A change in periapse altitude due to gravity perturbations may be tolerated, but a maneuver would most likely have to be performed if a dust storm was encountered.

All of the spacecraft events occur on a time line that is generated by ground personnel. These events take place at times relative to the predicted time of periapse. Errors in this prediction map into aerobraking maneuver (ABM) errors (thruster gravity losses). ABMs

[¶]Personal communication with R. Bishop, 2001.

are designed to occur in combination with specific spacecraft attitude configurations, mostly aligned with the velocity vector at apoapsis. Hence, a timing error would directly translate into an attitude error at the time of the burn, making it inefficient as compared with its design [6]. There were 32 ABMs performed over a 3-month span, on the Mars Odyssey mission.

During the drag pass, the spacecraft attitude is compared with a time-varying attitude profile (because the spacecraft attitude changes by approximately 40 deg over the entire drag-pass arc). Outside of the atmosphere (in the vacuum phase of the orbit), the spacecraft attitude is fixed (with the exception of ABM attitudes) such that the high-gain antenna is pointed at Earth. The attitude control authority is typically given to the reaction wheel assembly (RWA), but for the drag pass it is switched to the attitude control system (ACS) thrusters. A 20-deg dead band is usually allotted for tolerable nominal attitude offset during the drag pass. Historically, this 20-deg offset from the nominal attitude is equivalent to a timing error of approximately 225 s. Therefore, the navigation team must be able to predict subsequent periapse times to within this tolerance. Otherwise, propellant would be wasted due to the spacecraft thrusters having to fight against the aerodynamic torques. Figure 1 illustrates a typical long-orbit ($\sim$16 h orbit period) aerobraking navigation operations plan. In Fig. 1, P1 refers to periapsis-1 and A1 refers to apoapsis-1, where each number is associated with a specific orbit. The ordinate axis in the upper part of the figure represents altitude. The lower part of the figure is merely a cartoon representing the postperiapsis portion of the orbit where the navigation analysis and solution are computed.

The capability of the navigation team to predict subsequent periapse times is dominated by the atmospheric density uncertainty. For example (Mars Odyssey), assume an uncertainty of 35% (1σ). For large orbit periods, the expected change in period due to drag could be 1000 s. With a 105% (3σ) atmospheric density uncertainty, this means that the change in period could be off by 105%, in this case 1050 s, violating the 225 s timing error constraint. Therefore, during large orbit periods, the navigation team usually can not predict periapse time to within the 225 s constraint for more than one subsequent orbit as shown in Fig. 1. However, for the smaller orbits, where the expected period change could be as low as 30 s, with a 105% uncertainty, the navigation team can make predictions for many subsequent orbits [14].

The current navigation operations plan for aerobraking requires 24 hour-a-day staffing. Each drag pass is reconstructed, and there are daily meetings in order to make corridor control decisions. The orbit determination for aerobraking is as follows:

1) Obtain spacecraft initial conditions from the last solution (epoch starts at the beginning of tracking data received immediately following the preceding drag pass).

2) Obtain post-drag-pass attitude profile, atmosphere model inputs (baseline assumptions), and small-forces data (i.e., ACS thruster firings).

3) Collect tracking data from epoch (i.e., beginning of radiometric data immediately after the previous drag pass) up to approximately 1.5 h following the current drag pass. This 1.5 h accounts for the fact that tracking is not initiated until 30 min after periapsis and about 1 h of Doppler is processed and reduced post-drag pass, as seen in Fig. 1.

4) Reconstruct the drag pass for the orbit(s) by means of a radiometric data least-squares fit and save salient information (i.e., density, heat rate, etc).

5) Predict the trajectory of future orbits using the atmospheric model of choice (i.e., MarsGRAM).

6) Generate and deliver the orbit propagation and timing geometry (OPTG) and spacecraft ephemeris [SPK (Spice Kernel)] files to the appropriate servers/archival directories for use by science and engineering teams.

B. IMAN-Augmented Process

The way that inertial measurements for aeroassisted navigation (IMAN) were implemented in aerobraking follows:

1) Obtain the best estimate of spacecraft state and associated covariance before the drag pass.

2) Map (propagate) this state and covariance to the time of the initial IMU measurement and initialize IMAN with this as the a priori or initial conditions.

3) Reduce the IMU data with a sigma-point (unscented Kalman) filter, recovering estimates of spacecraft states and atmospheric density.

4) Following the reduction of the last IMU measurement, assess the effects of the drag pass by computing the peak dynamic pressure, heating rate, and periapsis altitude and comparing these to aerobraking corridor control strategies.

5) Propagate the last estimate of the state and covariance to predict the subsequent periapsis time and altitude.

III. Inertial Measurement Units

Nongravitational acceleration and inertial angular rate vector components used by IMAN are provided by the spacecraft IMU. The IMU on the Mars Odyssey contains three mutually orthogonal

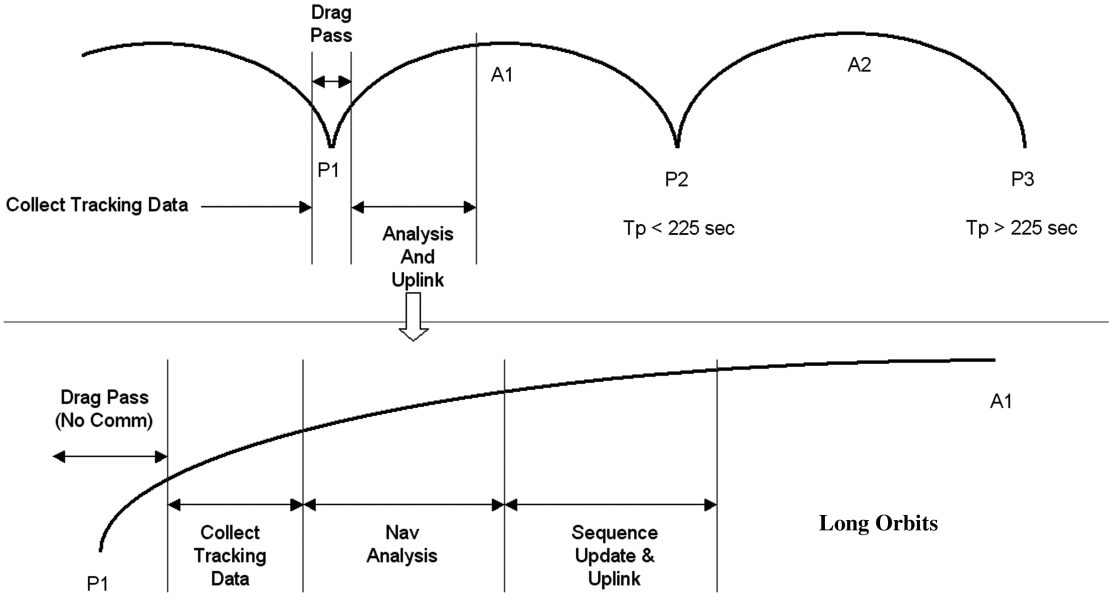

Fig. 1 Long orbit period aerobraking navigation strategy. This figure was taken from a Mars Odyssey Navigation PowerPoint presentation by Mase [13].

pendulous accelerometers and ring laser gyros (RLGs) directly mounted to the spacecraft (i.e., strapdown system).

For both accelerometers and gyroscopes, there are a number of error sources that corrupt the measurements; some of those** include 1) bias, 2) scale factor, 3) sensitivity, 4) nonlinearity, 5) repeatability, 6) misalignment/nonorthogonality, and 7) noise.

The model for the IMU (accelerometer and gyroscope) is defined by comparing [6] as follows. The gyroscope data are used as a deterministic truth model. Therefore, the gyroscope measurement model is not derived here. To calculate the measured acceleration in the IMU case frame ($\bar{a}_m^c$) let

$$\bar{a}_m^{\,c} = (I + \Lambda_a)(I + \Sigma_a)\left(\mathbf{T}_c^{\text{ric}}\bar{a}_{\text{nongrav}} + \mathbf{T}_c^{\text{body}}\bar{a}_{\text{rotation}} + \bar{b}_a + \bar{\varepsilon}_a\right) \tag{2}$$

where $\Lambda_a \equiv$ accelerometer misalignment/nonorthogonality errors (in the case frame), $\Sigma_a \equiv$ accelerometer scale factor errors (in the case frame), $\mathbf{T}_c^{\text{ric}} \equiv$ transformation matrix from radial in-track cross-track[††] to the case frame, $\bar{a}_{\text{nongrav}} \equiv$ nongravitational acceleration in the radial in-track cross-track frame, $\mathbf{T}_c^{\text{body}} \equiv$ transformation matrix from the body frame to the case frame, $\bar{a}_{\text{rotation}} \equiv$ spacecraft body frame acceleration induced in the IMU due to angular motion given that the IMU is not collocated with the spacecraft center of mass, $\bar{b}_a \equiv$ accelerometer bias (in the case frame), and $\bar{\varepsilon}_a \equiv$ uncorrelated accelerometer noise (white) sequence

$$\bar{a}_{\text{rotation}} = \dot{\bar{\omega}} \times \bar{r}_{\text{IMU}} + \bar{\omega} \times (\bar{\omega} \times \bar{r}_{\text{IMU}}) \tag{3}$$

where $\dot{\bar{\omega}} \equiv$ spacecraft body angular acceleration with respect to inertial space vector, $\bar{\omega} \equiv$ spacecraft body angular velocity with respect to inertial space vector and $\bar{r}_{\text{IMU}} \equiv$ IMU accelerometer triad position vector with respect to the spacecraft center of mass in spacecraft body frame.

To further describe Eq. (2), let

$$\begin{aligned} a_{\text{misalignment-}X} &= a_x\hat{x} + a_y\gamma_{xz}\hat{y} - a_z\gamma_{xy}\hat{z} \\ a_{\text{misalignment-}Y} &= -a_x\gamma_{yz}\hat{x} + a_y\hat{y} + a_z\gamma_{yx}\hat{z} \\ a_{\text{misalignment-}Z} &= a_x\gamma_{zy}\hat{x} - a_y\gamma_{zx}\hat{y} + a_z\hat{z} \end{aligned} \tag{4}$$

where $a_{\text{misalignment-}X} \equiv$ accelerometer misalignment in x axis of the case frame, $a_x \equiv$ nongravitational acceleration acting along x axis of the case frame, $\gamma_{xz} \equiv$ nonorthogonality coefficient of the x axis with respect to the z axis of the case frame with the other components similarly defined

Equation (4) can be further expressed and factorized as

$$\begin{bmatrix} a_{\text{misalignment-}X} \\ a_{\text{misalignment-}Y} \\ a_{\text{misalignment-}Z} \end{bmatrix} = \left\{ \begin{bmatrix} 1 & & \\ & 1 & \\ & & 1 \end{bmatrix} + \begin{bmatrix} 0 & \gamma_{xz} & -\gamma_{xy} \\ -\gamma_{yz} & 0 & \gamma_{yx} \\ \gamma_{zy} & -\gamma_{zx} & 0 \end{bmatrix} \right\} \begin{bmatrix} a_x \\ a_y \\ a_z \end{bmatrix} \tag{5}$$

where the accelerometer misalignment coefficients can be represented as

$$\Lambda_a = \begin{bmatrix} 0 & \gamma_{xz} & -\gamma_{xy} \\ -\gamma_{yz} & 0 & \gamma_{yx} \\ \gamma_{zy} & -\gamma_{zx} & 0 \end{bmatrix} \tag{6}$$

and the accelerometer scale factor errors can be represented as

$$\Sigma_a = \begin{bmatrix} \sigma_x & 0 & 0 \\ 0 & \sigma_y & 0 \\ 0 & 0 & \sigma_z \end{bmatrix} \tag{7}$$

where $\sigma_x \equiv$ accelerometer scale factor in x axis of the case frame with the other components similarly defined.

It is assumed that the accelerometer errors are represented by a zero mean white Gaussian noise sequence such that

$$E[\bar{\varepsilon}_a] = 0 \qquad E\left[\bar{\varepsilon}_a(t)\bar{\varepsilon}_a^T(\tau)\right] = \bar{R}_a(t)\delta(t-\tau) \tag{8}$$

where $E \equiv$ the expected value operator, $\bar{R}_a \equiv$ the measurement noise covariance and $\delta \equiv$ the Dirac delta function.

Assuming that the misalignment and scale factor errors are relatively small, then to first order we can say that

$$(I + \Lambda_a)(I + \Sigma_a) \approx I + \Lambda_a + \Sigma_a = I + \Delta_a \tag{9}$$

where

$$\Delta_a = \Lambda_a + \Sigma_a$$

Then

$$\bar{a}_m^{\,c} = (I + \Delta_a)\left(\mathbf{T}_c^{\text{ric}}\bar{a}_{\text{nongrav}} + \mathbf{T}_c^{\text{body}}\bar{a}_{\text{rotation}} + \bar{b}_a + \bar{\varepsilon}_a\right) \tag{10}$$

Therefore, in order to get the observed accelerations due to aerodynamic effects and using a first-order approximation to solve $(I + \Delta_a)^{-1}$:

$$\bar{a}_{\text{nongrav observed}} = \mathbf{T}_{\text{ric}}^{\text{c}}\left[(I - \Delta_a)\bar{a}_m^c - \left(\mathbf{T}_c^{\text{body}}\bar{a}_{\text{rotation}} + \bar{b}_a + \bar{\varepsilon}_a\right)\right] \tag{11}$$

where $\mathbf{T}_{\text{ric}}^{\text{c}} \equiv$ transformation matrix from the case frame to radial in-track cross-track.

IV. Inertial Measurements for Aeroassisted Navigation

Inertial measurements for aeroassisted navigation or IMAN is a set of MATLAB routines initially created and intended for use in the aerobraking phase of a flight project. IMAN processes and reduces IMU data as orbit-determination measurements. It estimates the translational and propagates the rotational states of a vehicle. Knowing that the trajectory reconstruction will be based on measurements that are noisy and potentially biased and use some given combination of kinematics and dynamics, the total-state vector formulation is partitioned in the following way:

$$\bar{X}_T = \begin{Bmatrix} X_k \\ X_{\text{pm}} \\ X_{\text{pd}} \end{Bmatrix} = \begin{Bmatrix} \text{6-element state subvector} \\ N_m\text{-element measurement model parameter subvector} \\ N_d\text{-element dynamics model parameter subvector} \end{Bmatrix}$$

The IMAN-state subvector X_k is defined as

$$\mathbf{X}_k = \begin{bmatrix} \text{s/c position} \\ \text{s/c velocity} \end{bmatrix} = \begin{bmatrix} x \\ y \\ z \\ \dot{x} \\ \dot{y} \\ \dot{z} \end{bmatrix}_{\text{MCI}}$$

where s/c is the spacecraft center and MCI is the Mars centered inertial (J2000[‡‡]) coordinate frame.

**Data available online at Honeywell Inertial Sensor Products, http://www.inertialsensor.com [retrieved 15 April 2005].

††The radial in-track cross-track frame is defined such that R is radially outward from the center of the central body through the spacecraft, C is along the orbit angular momentum vector, and I completes the orthogonal triad.

‡‡Let the J2000 frame be a body-centered inertial reference frame defined by the location of the mean equator and equinox on 1 Jan. 2000 12:00:00.000 Terrestrial Time (TT). This is equivalent to 1 Jan. 2000 11:58:55.816 UTC.

The IMAN measurement model parameter subvector X_{pm} is defined as

$$\mathbf{X}_{\text{pm}} = [C_{\text{drag}}]$$

where $C_{\text{drag}} \equiv$ spacecraft drag coefficient.

This parameter is both a measurement and a dynamic model parameter. These dynamics can be thought of as being caused by two distinct sources, gravitational and nongravitational. IMAN implements the point-mass and oblateness effects of the gravity field (truncated 20×20). The nongravitational model used is simply the equation of the acceleration due to drag defined by Eq. (12):

$$\bar{a}_{\text{drag}} = -C_{\text{drag}} \bar{q}_{\text{dp}} \frac{A_{\text{tot}}}{m} \tag{12}$$

$$\bar{q}_{\text{dp}} = \tfrac{1}{2}\rho |\bar{V}| \bar{V} \tag{13}$$

where a_{drag} is acceleration due to drag, q_{dp} is the dynamic pressure, ρ is the local density computed via Eq. (15), $\bar{V}$ is the local relative velocity vector, A_{tot} is the total area (contribution of projected areas), and m is the spacecraft mass.

However, V is the velocity relative to the atmosphere, which is rotating, therefore,

$$\bar{V} = \frac{\mathrm{d}\bar{r}}{\mathrm{d}t} - (\bar{\omega}_{\text{Mars}} \times \bar{r}) = \begin{bmatrix} \frac{\mathrm{d}x}{\mathrm{d}t} + \omega_{\text{Mars}} y \\ \frac{\mathrm{d}y}{\mathrm{d}t} - \omega_{\text{Mars}} x \\ \frac{\mathrm{d}z}{\mathrm{d}t} \end{bmatrix} \tag{14}$$

where $\mathrm{d}\bar{r}/\mathrm{d}t \equiv$ the spacecraft inertial velocity vector (with components x, y, z); $\bar{\omega}_{\text{Mars}} \equiv$ the angular velocity vector for Mars; and $\bar{r} \equiv$ the spacecraft inertial position vector (with components x, y, z).

A 5-parameter exponential atmosphere model is used in this research [5]. The modeled density is computed as

$$\rho_{\text{computed}} = \rho_o e^{-C_1 \frac{h}{H_o} + C_2 \cos(\frac{2\pi h}{H_o}) + C_3 \sin(\frac{2\pi h}{H_o})} \tag{15}$$

where $\rho_o \equiv$ exponential atmospheric base density; C_1, C_2, $C_3 \equiv$ exponential atmosphere coefficients derived as indicated by [6]; $h \equiv$ altitude above the planet surface; and $H_o \equiv$ exponential atmospheric scale height.

In a traditional exponential atmosphere model, C_1 is equal to one and the other two coefficients are zero. When the nongravitational accelerations are root-sum squared (RSS), the result is effectively the acceleration due to drag. The lift and side forces are not modeled and are approximately 2 orders of magnitude smaller than the drag acceleration. Solar pressure effects were not modeled because they amount to approximately 5 orders of magnitude less than the drag acceleration.

The attitude is not estimated during aerobraking because there are no external attitude measurements made throughout the drag pass. The spacecraft body rates derived from the gyroscope measurements are used directly in the attitude dynamic model (the gyroscope measures increments of integrated angular rates over each sample period not attitude quaternions). Therefore, one is left with estimating for translation states and deduced reckoning for rotation states. The attitude is propagated via the numerical integration of the quaternion derivative by means of Eq. (16) compared to [15]

$$\dot{\mathbf{q}} = \frac{1}{2}\Omega\bar{\omega} = \frac{1}{2}\begin{bmatrix} -q(2) & -q(3) & -q(4) \\ q(1) & -q(4) & q(3) \\ q(4) & q(1) & -q(2) \\ -q(3) & q(2) & q(1) \end{bmatrix}_{\text{inertial}}^{\text{body}} \begin{bmatrix} \omega_x \\ \omega_y \\ \omega_z \end{bmatrix}_{\text{body}} \tag{16}$$

where $q(1)$ is the scalar term, $q(2\text{–}4)$ is the vector term, and ϖ is the body-rate vector.

Initially, IMAN employed an extended Kalman filter (EKF) to drive the state estimation process. However, some of the drawbacks of the EKF are that it only works well with systems that are near linear on the time scale of the measurement updates [16], it requires Jacobians of relationships that can be very complicated to implement, and these filters can also be notoriously cumbersome to tune. Tuning a filter refers to the process of selecting the appropriate measurement noise, process noise, and other parameters to which the filter output is sensitive, which yield acceptable state estimates. At a basic level, what is tuned is the Kalman gain, to yield the optimal state estimate. These reasons have motivated novel approaches in nonlinear system estimation. One such method was introduced by [16] called the unscented Kalman filter (UKF). IMAN has the UKF as its baseline filter strategy.

Several benefits of the UKF are that no explicit derivatives (Jacobians) are required [17,18], no linearization is required, and the dynamics are propagated through their modeled nonlinearities. Given an a priori mean and covariance, a set of points (states) is sampled. Although similar to a Monte Carlo, the difference lies in that the sampled points are not being randomly drawn based upon the a priori statistics but rather drawn based upon a minimum set of deterministically chosen weighted points, which completely capture the true mean and covariance of the prior random variable [19]. When these points, called sigma points, are propagated through the modeled nonlinear system, the a posteriori mean and covariance are captured accurately to the second order for any nonlinearity. For Gaussian distributions, third-order accuracies are expected. The UKF algorithm implemented by IMAN can be summarized in the following numbered steps:

Let $L=$ be the number of state parameters.

1) Choose α, where $1e-4 < \alpha < 1$ primary scaling factor minimizing higher-order effects, chosen to be 1.0 in this analysis; κ secondary scaling parameter, usually set to 0 for state estimation and $3 - L$ for parameter estimation [18]; and $\beta = 2$, optimal for Gaussian distributions [18].

2) Compute weights

$$\begin{gathered} W_0^m = \lambda/(L+\lambda) \qquad W_0^c = \lambda/(L+\lambda) + (1-\alpha^2+\beta) \\ W_i^m = W_i^c = 1/\{2(L+\lambda)\} \qquad i = 1, \ldots, 2L \end{gathered} \tag{17}$$

where $\lambda = \alpha^2(L+\kappa) - L$ and $\gamma = \sqrt{(L+\lambda)}$. Note that $L + \lambda = 3$ is well-suited for a Gaussian assumption of the state errors [17].

3) Initialize the UKF given

$$P_{t-1}, \hat{X}_{t-1}, R_t$$

4) Compute sigma points (matrix) for $t-1$:

$$\chi_{t-1} = [\,\hat{X}_{t-1} \quad \hat{X}_{t-1} + \gamma\sqrt{P_{t-1}} \quad \hat{X}_{t-1} - \gamma\sqrt{P_{t-1}}\,]_{Lx(2L+1)} \tag{18}$$

5) Propagate sigma points through nonlinear system

$$\chi_{t/t-1} = F(\chi_{t-1}, \mathbf{u}_{t-1}) \tag{19}$$

where $\mathbf{u}_{t-1}$ is a known exogenous input (for this research, the thruster firings occurring during the drag pass fall into this category).

Note: This implies integrating $2L + 1$ state vectors at each time step (i.e., each column).

6) Perform a state and covariance time update

$$\bar{X}_t = \sum_{i=0}^{2L} W_i^m \chi_{i,t/t-1} \tag{20}$$

$$\bar{P}_t = Q + \sum_{i=0}^{2L} W_i^c (\chi_{i,t/t-1} - \bar{X}_t)(\chi_{i,t/t-1} - \bar{X}_t)^T \tag{21}$$

where Q is the process noise covariance.

7) Recompute sigma points to incorporate effects of process noise

$$\chi_{t/t-1} = [\,\bar{X}_t \quad \bar{X}_t + \gamma\sqrt{\bar{P}_t} \quad \bar{X}_t - \gamma\sqrt{\bar{P}_t}\,]_{Lx(2L+1)} \tag{22}$$

8) Compute the measurements associated with each sigma-point vector and their weighted averages

$$Y_{t/t-1} = G(\chi_{t/t-1}) \qquad \bar{y}_t = \sum_{i=0}^{2L} W_i^m Y_{i,t/t-1} \tag{23}$$

9) Compute the innovation and cross-correlation covariances

$$P_{yy} = R + \sum_{i=0}^{2L} W_i^c (Y_{i,t/t-1} - \bar{y}_t)(Y_{i,t/t-1} - \bar{y}_t)^T \tag{24}$$

$$P_{xy} = \sum_{i=0}^{2L} W_i^c (\chi_{i,t/t-1} - \bar{X}_t)(Y_{i,t/t-1} - \bar{y}_t)^T \tag{25}$$

10) Compute the Kalman gain, the best estimate of the state, and the a posteriori state covariance

$$K_t = P_{xy} P_{yy}^{-1} \qquad \hat{X}_t = \bar{X}_t + K_t(y_t - \bar{y}_t) \qquad P_t = \bar{P}_t - K_t P_{yy} K_t^T \tag{26}$$

where y_t are the IMU measurements.

11) Return to step 4 until all the observations have been processed.

V. Results from Mars Odyssey Aerobraking

IMU data were processed and reduced in several state estimation methods based on simulated scenarios. Once the simulated scenarios produced acceptable results, the next step was to ascertain whether or not flight data could be successfully processed. The Odyssey orbiter performed 3 months of aerobraking, beginning with a 19-h orbit and aerobraking down to a 2-h orbit. One could characterize the aerobraking orbits into 3 types of orbit regimes: large, medium, and small. A robust IMU navigation tool should be able to perform well in all 3 aerobraking regimes. Thus, data from orbits with periods near 16 h (P-22), 6 h (P-104), and 2 h (P-329) were analyzed using IMAN. This nomenclature refers to the orbit after the numbered periapsis (i.e., P-22 refers to orbit after periapsis 22). For the Mars Odyssey, P-1 occurred during the Mars orbit insertion burn. IMAN processes and reduces IMU data as orbit-determination measurements; it comprises a sigma-point filter that estimates the translational and propagates the rotational states of a spacecraft.

The IMU data obtained from the spacecraft team at Lockheed Martin Space Systems was adjusted in the following way: 1) corrected for rollover, 2) converted from IMU case frame to the spacecraft body frame, 3) converted into engineering units (velocities and angles), 4) corrected for biases, 5) converted to accelerations and angular rates, 6) corrected for accelerometer-sensed angular motion-induced accelerations. Because the accelerometers are not collocated with the spacecraft center of mass, angular motion will induce a linear acceleration sensed by the accelerometers.

Figure 2 illustrates the Mars Odyssey aerobraking configuration. The IMU measurements begin well before and after the drag pass, in a region where the output should be null. This allows for the identification of the bias.

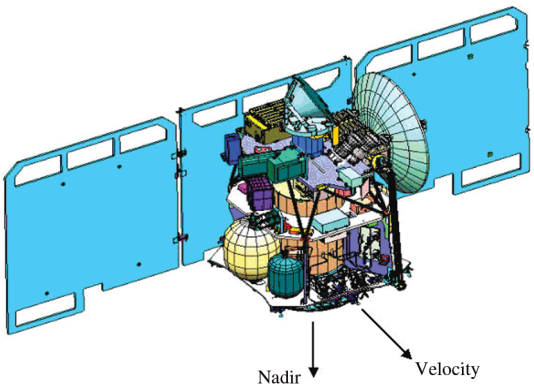

Fig. 2 Mars Odyssey normal aerobraking configuration [15]. Spacecraft axes: +Z (radial or antinadir), +X (cross-track), +Y (anti-in-track or antivelocity).

The simulated data analysis indicated that there was little value in processing and reducing IMU data in orbital regimes above 130 km in altitude. It is worth noting that this might not be the case with a more sensitive IMU, such as one that could measure accelerations on the order of solar radiation pressure. Given the Odyssey IMU measurement accuracy, the IMU data used were truncated to that within 130 km from the surface. The manner in which IMAN was implemented for Odyssey follows:

1) The navigation team produced a pre-drag-pass best estimated spacecraft state and associated covariance based upon a radiometric data reduction collected in the vacuum phase of the orbit.

2) Both the best estimated state and its associated full covariance were then mapped forward to the time coinciding with the first IMU measurement within this truncated IMU data set.

3) The mapped epoch state and covariance were then loaded into IMAN.

4) Another file obtained from the archived Odyssey aerobraking data set was the associated small forces file (SFF). This file contains data associated with spacecraft center of gravity (CG) ΔV increments and burn durations (Δt) in J2000 coordinates resulting from thruster-firing events. The SFF also contains an associated inertial-to-body spacecraft attitude quaternion for each thrusting event.

5) The parsed SFF was loaded into IMAN, and at the appropriate event end times the propulsive information was applied to the spacecraft position and velocity states as shown in Eq. (27).

6) In IMAN, the current-time numerically integrated quaternion was replaced by the quaternion on the SFF. Every aerobraking orbit had an associated SFF. One of the main reasons for these drag-pass thruster firings was the desaturation of the reaction wheels. A free angular momentum desaturation (AMD) can be achieved in two of the three spacecraft axes. Aerodynamic forces keep the spacecraft stable in pitch and yaw, and these forces are strong enough to allow for the commanded despinning of the reaction wheels without imparting angular motion to the spacecraft. Because this is not necessarily true for the roll axis, this axis is typically desaturated by the use of the ACS thrusters.

7) Once the last IMU measurement is processed, the best estimated state and covariance from IMAN are mapped forward to the time of the first post-drag-pass radiometric measurement.

8) This mapped post-drag-pass state and covariance are now directly compared with the navigation team solution at this time, based upon the navigation team's reduction of at least 1 h of post-drag-pass radiometric data

$$\mathbf{X}_{\text{updated}} = \mathbf{X}_{\text{current}} + \Delta\mathbf{X} = \begin{bmatrix} x + 1/2\Delta V_x \Delta t \\ y + 1/2\Delta V_y \Delta t \\ z + 1/2\Delta V_z \Delta t \\ \dot{x} + \Delta V_x \\ \dot{y} + \Delta V_y \\ \dot{z} + \Delta V_z \end{bmatrix} \tag{27}$$

where $\Delta V_x \equiv$ the change in velocity given by the propulsive maneuver in the inertial x direction (the other components are similarly defined) and $\Delta t \equiv$ the time interval during which the propulsive maneuver took place

A. Large Orbits (P-22)

An orbit representative of a large orbit is P-22, with roughly a 16-h period. The duration of the effective drag pass for this orbit is on the order of 350 s, which is fairly short compared with the smaller orbits ($\sim$2 h period) whose drag-pass durations are on the order of 1000 s. It should be noted that the amount of ΔV removed from every orbit is approximately the same by design, because the dynamic pressure corridor constraints are fairly constant throughout aerobraking. This neglects endgame, which has an orbit lifetime constraint based on the integrated heating effect rather than a fixed heating rate limit that maps to a dynamic pressure limit.

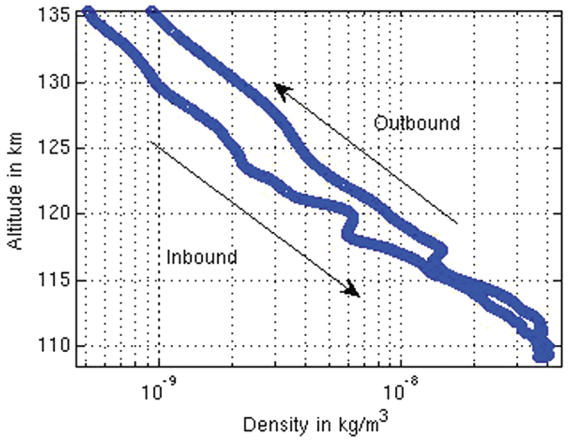

Fig. 3 Altitude vs density profile reconstructed from IMU data reduction for P22 using the UKF.

Navigation is primarily interested in the overall effect of drag on the orbit, which is not a driver for improving the atmosphere model so long as the next periapsis time can be predicted to within the 225-s constraint. However, with an increasing demand for better navigation through low Mars orbits, there is a great benefit to improving our understanding of Mars' atmospheric behavior. This motivates the real-time reconstruction of the atmosphere and is a benefit from processing and reducing IMU data collected throughout the drag pass. Figure 3 shows the reconstructed density profile, from the IMU data reduction, for P22. The filtering strategy used for the results shown was the UKF, a specific form of the more commonly known sigma-point filter [17,18]. The results obtained by the EKF are very similar, and showing them would be redundant. To reconstruct the actual density, the magnitude of the acceleration due to drag was saved at each time step. This was calculated as follows:

$$a_{\text{drag}} = -\frac{1}{2}\rho_{\text{computed}} V^2 C_{\text{drag-estimated}} \frac{A}{m} \tag{28}$$

Once this acceleration was computed, then an actual density was solved using the known C_{drag} value of 2.1 as follows:

$$\rho_{\text{reconstructed}} = -\frac{2a_{\text{drag}} m}{|\bar{V}|^2 A C_{\text{drag-known}}} \tag{29}$$

Inbound and outbound, in Fig. 3, refer to the path in and out of the atmosphere that was negotiated by the spacecraft. What is interesting about this plot is the structure that can be seen in the density near periapsis. This structure is real [20]. The Mars Odyssey Atmospheric Advisory Group (which included [20]), theorized that a polar vortex existed at the Mars north pole, and this phenomena, affecting the local density, was visible in the IMU data. This group also held that there were longitude-dependent density waves and that density variation near periapsis could be up to 40% within a few seconds.

The advantage in reconstructing the density with this filtering technique vs matching IMU data with the navigation trajectory is that the navigation trajectory has no data through the atmosphere so that it cannot reflect the real-time changes that take place in the atmosphere. The navigation trajectory is the best estimated state based on data before and after the drag pass, not during the drag pass. This is where processing IMU data as a navigation measurement and reducing a trajectory to these data in real time (or in a current-state filter), allows for a more realistic atmospheric structure to be recovered. This in turn, in the hands of atmospheric scientists, becomes the information needed to produce realistic improvements to current atmosphere models. To quantify how well the density can be recovered and at what altitudes this density is practically immeasurable, Fig. 4 shows the reconstructed density signal-to-noise ratio (SNR) for P22, generated via Eq. (31). The method by which the SNR is computed at each time step follows.

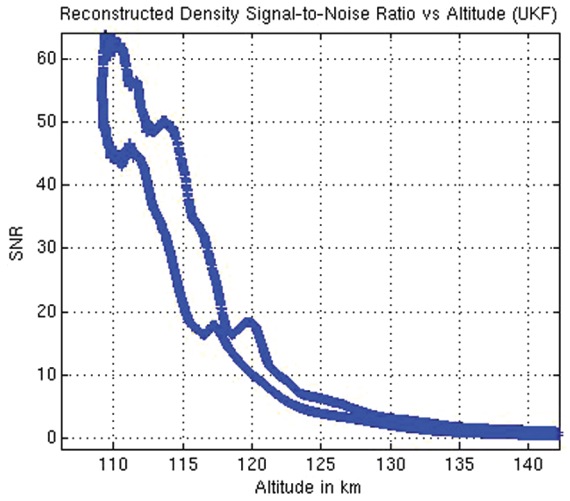

Fig. 4 Reconstructed density signal-to-noise ratio (SNR) for P22 (UKF).

First, rotate the MCI-frame root-mean square (rms)of the nongravitational acceleration residuals to the radial in-track cross-track (RIC) frame:

$$\mathbf{rms}_{\text{RIC}} = \mathbf{T}_{\text{RIC}}^{\text{MCI}} \mathbf{rms}_{\text{MCI}}$$

Because the density is based upon the drag accelerations, use the in-track rms value (rms_I). Scale this by three in order to get an SNR of one for a density reconstructed value that is right at the 99% threshold of all noise values:

$$a_{\text{noise}} = 3\mathbf{rms}_I$$

Then, for this equivalent acceleration due to drag, compute the density value:

$$\rho_{\text{noise}} = -\frac{2a_{\text{noise}} m}{|\bar{V}|^2 C_{\text{drag}} A} \tag{30}$$

Finally, SNR is computed by taking the reconstructed density in Eq. (29) and dividing it by Eq. (30):

$$\text{SNR} = \frac{\rho_{\text{reconstructed}}}{\rho_{\text{noise}}} \tag{31}$$

As can be seen from Fig. 4, the SNR is fairly close to zero around 150 km in altitude. It is not until around 135 km from the surface that the SNR becomes larger than two. This implies that confidence in density estimates above this altitude should be very low because the signal is in the noise. Alternatively, it is interesting to note that the structure seen in the density reconstruction is very observable from an SNR perspective.

To directly compare the observations with the computed values, Figs. 5–7 show the observed vs computed quantities in the radial, in-track, and cross-track directions. The discontinuities observed in Figs. 5 and 7 are the products of nearly 50 thruster-firing attitude updates that occurred during the P22 drag pass. The lift and sideforce are not being modeled explicitly. Although they are very small compared with the drag force, this still produces some level of mismodeling. Another point to note is that the thruster firings are assumed to be perfectly known in this analysis. In reality, there is some level of error in the thruster pulses themselves, and the information given to the navigation team within the small forces file may be biased. Typically, the navigation team estimates a stochastic scale factor applied to the small force data in order to account for these errors. This scale factor is not being estimated here and is a potential source of improvement of these results.

Figure 6 shows the drag pulse for P22. As can be seen, the observed and computed quantities lay on top of each other. The structure seen in this figure reflects true variations in the Mars

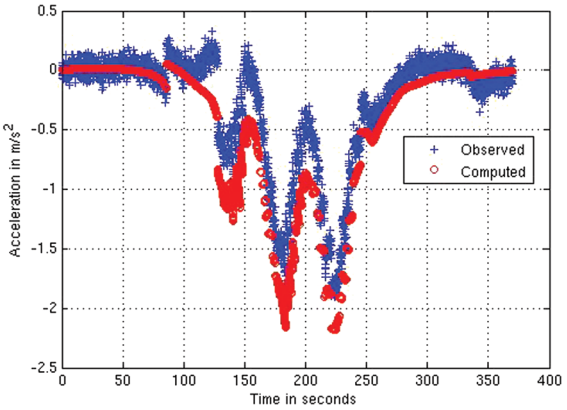

Fig. 5 Observed vs computed nongravitational accelerations in the radial direction for P22 (UKF).

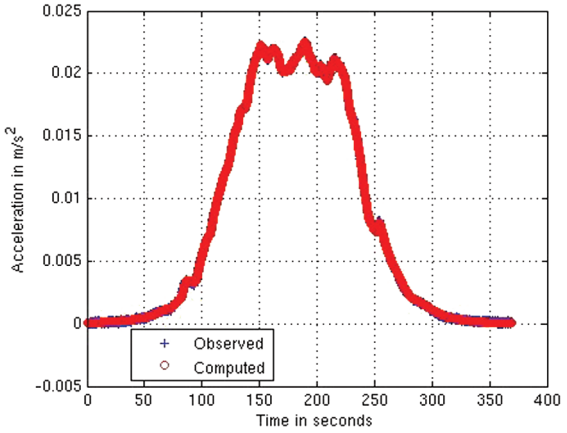

Fig. 6 Observed vs computed nongravitational accelerations in the (-) in-track direction for P22 (UKF).

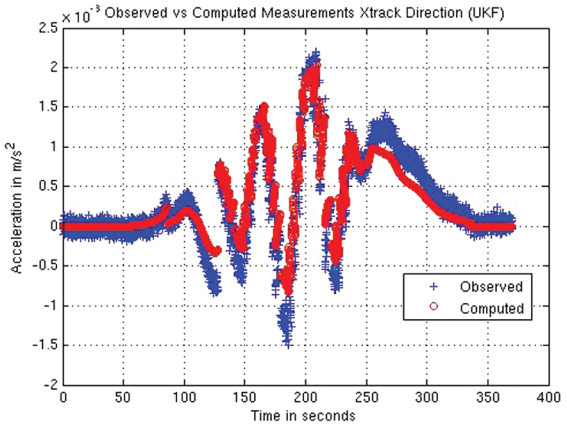

Fig. 7 Observed vs computed nongravitational accelerations in the cross-track direction for P22 (UKF).

atmosphere during the drag pass. Interesting to note are the two "humps" entering and leaving the atmosphere. Atmospheric scientists theorized that there was a polar vortex evident in the data around these early orbits because periapsis precessed through the Mars north pole due to oblateness effects[§§] [20].

The Jet Propulsion Laboratory navigation team uses a tool called DIZZY, which differences states and provides this in a summary format. A brief description of relevant parameters on the differenced-state file is provided in Table 1.

[§§]Personal communication with Richard Zurek (2005).

Table 1 Differenced-state file parameter description

Description	Parameter name
Absolute position difference	|pos|
Absolute velocity difference	|vel|
Semimajor axis	SMA
Period	PRD
Radial position component in RIC frame	V1Rad
In-track position component in RIC frame	V1DTrk
Cross-track position component in RIC frame	V1Nrml
Radial velocity component in RIC frame	V1RadD
In-track velocity component in RIC frame	V1DTrkD
Cross-track velocity component in RIC frame	V1NrmlD

To conclude the results for these larger aerobraking orbits, Tables 2–4 show the performance of the various filter strategies against the navigation team's (NAV) solution. These differences are reflected at a fixed time. For clarity in Table 2 NAV-IMU is the difference between the navigation team's state solution and what one achieves by using the IMU measurements directly in lieu of the nongravitational force model. NAV-batch is the difference between the navigation team's state solution and what one achieves by using a differential correction (or least squares) data reduction technique. NAV-EKF and NAV-UKF are these differences from extended and unscented Kalman filters, respectively.

As can be seen from Table 2, the batch does an acceptable job, yet not as well as the EKF and UKF, which compare very well with each other. This is to be expected from the batch because the drag-pass nonlinearities are captured better by the current-state filters and the direct inclusion of the IMU data as part of the dynamic model.

Another measure of how well IMAN performed can be found in comparing the maximum dynamic pressures and heat rates. These two parameters are the key to aerobraking corridor control strategies and operations. Violating either side of the corridor will incite an action from the operations team. Not experiencing enough drag may prompt a periapse-lowering maneuver. The less benign side, experiencing too much drag, will prompt a periapse-raising maneuver. The ability of IMAN to satisfactorily detect the maximum heating rate and dynamic pressure is crucial if it is to be relied upon during aerobraking operations. Table 3 shows the comparison between the NAV and IMAN reconstructed values of these parameters. IMAN is able to detect these quantities to within 5% of the navigation team solution. In fact, it may be arguable that IMAN is more correct, given that the IMU directly measures the dynamics that determine these parameters.

Figure 8 shows results from the Odyssey Atmospheric Advisory Group (AAG) for P22. Quantitatively, it compares well with the IMAN results (Fig. 3). Qualitatively, IMAN shows higher resolution of the density structure. This, in part, is due to the fact that the AAG solution is using 39 s averaged data, whereas IMAN reduces IMU data at 10 Hz.

Finally, a comparison in the ability to predict the subsequent periapse time and altitude between NAV and IMAN can be seen in Table 4. There is no formal requirement for periapse altitude prediction although the timing requirement is 225 s. However, predicted density values are highly correlated with periapsis altitude predictability. For clarity in Table 4 NAV-predicted IMAN is the difference between the navigation team's predicted time and altitude of the subsequent periapsis and the prediction given by IMAN. NAV-reconstructed IMAN is the difference between the navigation team's reconstructed time and altitude of the subsequent periapsis and the prediction given by IMAN. This reconstruction includes radiometric data obtained after periapse passage. This may be viewed as the navigation team solution after the fact vs IMAN before the fact. NAV-predicted/NAV-reconstructed shows the navigation team's difference between pre-drag-pass and post-drag-pass estimates.

IMAN is within several seconds and meters from the NAV values. It is shown that there is no need for post-drag-pass radiometric data to successfully determine subsequent periapse quantities, if implementing IMAN. It must be noted that IMAN would eventually need

Table 2 NAV vs IMAN solution comparison for P22

Parameter	NAV-IMU	NAV-batch	NAV-EKF	NAV-UKF
|pos|, km	0.031	0.060	0.030	0.033
|vel|, cm/s	6.664	7.686	3.231	3.980
SMA, km	−1.230	4.017	−1.365	−0.880
PRD, hours:minutes:seconds	−00:00:06.96	−00:00:22.73	−00:00:07.72	00:00:04.97
V1Rad, km	−0.008	0.017	−0.001	0.007
V1DTrk, km	0.028	0.055	0.026	0.026
V1Nrml, km	−0.012	−0.017	−0.016	−0.019
V1RadD, cm/s	−6.556	4.066	−1.625	1.161
V1DTrkD, cm/s	−1.066	6.096	−2.376	−2.337
V1NrmlD, cm/s	−0.543	−2.317	−1.468	−3.005

Table 3 Maximum dynamic pressure and heat rate comparison between NAV and IMAN for P22 (UKF)

Drag-pass parameter	NAV	IMAN
q_{max}, N/m^2	0.466	0.443
$qdot_{max}$, W/cm^2	0.218	0.207

Table 4 NAV vs IMAN subsequent periapsis condition comparison for P22 (UKF)

Subsequent periapsis statistics	Timing, s	Altitude, m
NAV-predicted IMAN	−5.124	−3.653
NAV-reconstructed IMAN	−4.976	−4.351
NAV-predicted/NAV-reconstructed	0.148	−0.697

to be reinitialized with an updated radiometric solution as errors would accumulate in time and reach a point where IMAN is likely to be unable to recover state errors. Determining how long IMAN could be relied upon without being reinitialized with a radiometric solution (i.e., use the same a priori state and associated covariance for multiple orbit revolutions), would be a worthwhile pursuit for future work.

The performance achieved from processing IMU data during medium- and smaller-sized orbits is similar to that shown for the larger orbit (P22). Therefore what follows are tables summarizing this performance for the two other orbit regimes.

B. Medium Orbits (P-104)

Table 5 shows the performance of the various filter strategies against the NAV solution for P104. Note that, as is consistent with the a priori state uncertainties, the largest deviations from the navigation solution are in-track position and radial velocity.

The batch does an acceptable job, yet not as good as the EKF and UKF that compare very well with each other. Using the IMU as a replacement for the atmosphere model yields better results commensurate with the UKF. These results are provided in

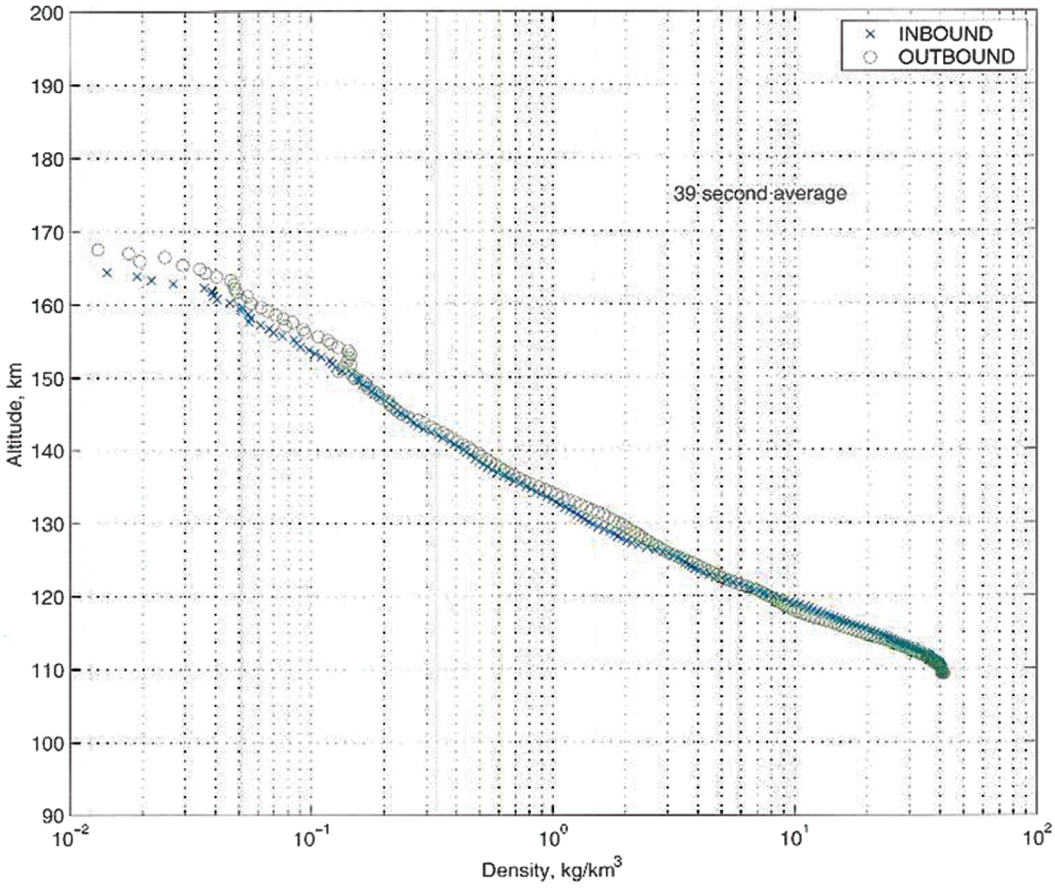

Fig. 8 Accelerometer Advisory Group (AAG) reconstructed density profile (P22).

Table 5 NAV vs IMAN solution comparison for P104

Parameter	NAV-IMU	NAV-Batch	NAV-EKF	NAV-UKF
|pos|, km	0.170	0.157	0.167	0.170
|vel|, cm/s	32.704	70.065	28.966	24.638
SMA, km	−0.253	−7.812	−0.314	0.047
PRD, hours:minutes:seconds	−00:00:01.02	−00:00:32.42	−00:00:01.27	00:00:00.19
V1Rad, km	−0.016	0.004	−0.016	−0.006
V1DTrk, km	0.169	0.157	0.166	0.170
V1Nrml, km	0.008	0.003	−0.002	−0.008
V1RadD, cm/s	−28.055	-33.434	−26.121	−22.548
V1DTrkD, cm/s	2.310	−59.434	1.599	3.226
V1NrmlD, cm/s	16.647	16.091	12.415	9.393

differenced-state files seen in the preceding figures. Another measure of how well IMAN performed can be found in comparing the maximum dynamic pressures and heat rates. Table 6 shows the comparison between the NAV and IMAN reconstructed values of these parameters.

Although IMAN is within 14% of the navigation team solution, this should not be alarming. There are orbits where the spacecraft team at Lockheed Martin had up to 300% differences with the navigation team. Again, it should be noted that IMAN directly measures the atmospheric dynamics that determine these parameters. Finally, a comparison in how well the subsequent periapse time and altitude are predicted follows in Table 7.

IMAN is only within tenths of a second and just over a meter from the NAV values. It is shown that IMAN can successfully determine subsequent periapse quantities.

C. Small Orbits (P-329)

Table 8 shows the performance of the various filter strategies against the NAV solution for the smaller orbit P329.

Although the batch has been shown to yield less accurate results, it should be noted that the performance of the batch processor is in part levied upon the modeling capability employed by this strategy. Process noise can be incorporated in the current-state filters in a straightforward manner. This is not true for the batch. Table 9 shows the comparison between the NAV and IMAN reconstructed values of both the maximum dynamic pressure and heating rate for P329.

Once more, IMAN is able to detect these quantities to within a few percent of the navigation team solution. The subsequent periapsis conditions' comparison between NAV and IMAN follows in Table 10.

IMAN shows that it can be relied upon for successfully determining these quantities. IMAN has performed satisfactorily across all orbit regimes.

VI. Conclusions

The research shows that filtering IMU data during aerobraking yields comparable post-drag-pass state estimates, reconstructed density profiles, and subsequent periapsis time and location estimates. There are benefits to processing and reducing the IMU data in IMAN. These benefits include: 1) a realistic associated uncertainty along with the state, based upon the IMU data, 2) obtaining density reconstruction estimates for use for possible

Table 6 Maximum dynamic pressure and heat rate comparison between NAV and IMAN for P104 (UKF)

Drag-pass parameter	NAV	IMAN	% difference
q_{max}, N/m^2	0.733	0.631	13.9
$qdot_{max}$, W/cm^2	0.323	0.277	14.2

Table 7 NAV vs IMAN subsequent periapsis condition comparison for P104 (UKF)

Subsequent periapsis statistics	Timing, s	Altitude, m
NAV-predicted IMAN	0.193	−1.348
NAV-reconstructed IMAN	0.211	−1.267
NAV-predicted/NAV-reconstructed	0.017	0.082

Table 9 Maximum dynamic pressure and heat rate comparison between NAV and IMAN for P329 (UKF)

Drag-pass parameter	NAV	IMAN	% difference
q_{max}, N/m^2	0.051	0.052	1.9
$qdot_{max}$, W/cm^2	0.141	0.146	3.5

Table 10 NAV vs IMAN subsequent periapsis condition comparison for P329 (UKF)

Subsequent periapsis statistics	Timing, s	Altitude, m
NAV-predicted IMAN	1.050	9.200
NAV-reconstructed IMAN	1.495	−3.856
NAV-predicted/NAV-reconstructed	0.389	13.058

Table 8 NAV vs IMAN solution comparison for P329

Parameter	NAV-IMU	NAV-batch	NAV-EKF	NAV-UKF
|pos|, km	0.437	0.406	0.441	0.426
|vel|, cm/s	35.647	57.289	38.398	39.792
SMA, km	0.015	0.005	−0.003	0.053
PRD, hours:minutes:seconds	−00:00 : 00.04	00:00:00.01	−00:00:00.00	00:00:00.14
V1Rad, km	−0.110	0.094	−0.115	−0.104
V1DTrk, km	−0.422	−0.394	−0.426	−0.413
V1Nrml, km	0.032	0.018	0.009	0.006
V1RadD, cm/s	24.085	49.413	24.596	25.639
V1DTrkD, cm/s	10.542	−10.169	10.234	11.554
V1NrmlD, cm/s	−24.072	−27.146	−27.653	−28.152

model atmospheric model improvement, and 3) a method that is robust in the presence of an IMU data outage.

The results achieved by IMAN (which does not incorporate post-drag-pass data) are comparable to the navigation solution, which includes post-drag-pass radiometric data. This indicates that IMAN provides a reliable independent assessment of the drag-pass dynamics without the need for further radiometric data processing. Typically, the navigation team is allotted 3 h past periapsis to collect and reduce radiometric data and deliver trajectory products to engineering and science teams. IMAN achieves its results in an amount of time equivalent to the sensed drag pass using a current-state filter.

Spacecraft events, such as slewing to and from drag-pass attitudes, take place relative to the predicted periapse times, which are required to be within 225 s in error. Because periapsis altitude is highly correlated with atmospheric density and, thus, the dynamic pressure experienced by the spacecraft, it is in the interest of the navigation team to minimize periapse altitude uncertainties. This error is typically constrained to 1.5 km [7]. The research shows that IMAN can be used to reliably predict subsequent periapsis times to within several seconds and locations to within several meters, over all representative aerobraking regimes.

During aerobraking, a dynamic pressure or heating rate corridor is defined so as to meet mission requirements and keep the spacecraft from potentially burning up in the atmosphere. If the spacecraft violates the heating rate upper corridor limit, then a periapse-raising maneuver must be commanded and successfully implemented in order to insure mission safety. The research shows that IMAN also yields accurate peak dynamic pressure and heating rates, critical for a successful corridor control strategy, matching navigation team values to within several percent.

A cornerstone of aerobraking operations is the participation of the Atmospheric Advisory Group (AAG), composed of expert interplanetary atmospheric scientists. These experts attempt to characterize the atmosphere on a daily basis, with the intent of refining current atmospheric models. IMAN is shown to produce consistent, reconstructed density profiles,[¶] as compared with AAG results archived during the Mars Odyssey aerobraking phase. The IMAN density reconstructions have a greater resolution than previously achieved by the AAG. This is because of the fact that accelerometer measurements collected by the AAG were coupled to spacecraft states based on the navigation solution, which was a least-squares fit through the drag pass. IMAN, being a current-state filter, produces state estimates achieved by reducing the accelerometer data and yields reconstructed density values coincident with each measurement. Therefore, the density profile has a resolution equivalent to the measurement time span, in this case at every 0.1 s.

This research provides the first instance of the utilization of the UKF for the purpose of estimating an actual spacecraft trajectory arc about another planet. The UKF produced consistent results across the various orbit regimes and delivered realistic covariances. It must be noted that although the results obtained from a specific orbit may be improved with fine tuning, the research proved that a robust filter strategy can be successfully employed because the filter parameters were maintained constant across all aerobraking regimes, yielding navigation-grade results.

Acknowledgments

The work described in this paper was carried out at the Jet Propulsion Laboratory, California Institute of Technology, under a contract with the National Aeronautics and Space Administration. Reference herein to any specific commercial product, process, or service by trade name, trademark, manufacturer, or otherwise, does not constitute or imply its endorsement by the United States Government or the Jet Propulsion Laboratory, California Institute of Technology. The authors acknowledge the assistance of those individuals who made this research possible: Dan Lyons, whose initial funding helped get this research underway; Joe Guinn, who helped with the conception of this research topic; Dolan Highsmith, who was used relentlessly as a sounding board for this research; Tung-Han You, whose insight and grasp of the problem served as a well-calibrated set of independent eyes that assisted in seeing solutions to the problem; Dan Burkhart, Cassaundra Jah, and AIAA anonymous reviewers, for taking time away from personal tasks in order to review this body of work; and Jay Wyatt for channeling the funding necessary to see this research through to a meaningful end.

[¶]Personal communication with Richard Zurek (2005).

References

[1] Jah, M. K., "A Proposed Use of Accelerometer Data for Autonomous Aerobraking at Mars," AIAA/AAS Astrodynamics Specialist Conference, American Astronautical Society Paper 01-386, Quebec City, Canada, July 2001.

[2] Jah, M. K., and Lisano, M. E., II., "6-DOF Aerobraking Trajectory Reconstruction by Use of Inertial Measurement Unit (IMU) Data for the Improvement of Aerobraking Navigation," 14th Space Flight Mechanics Meeting, American Astronautical Society Paper 04-214, Maui, HI, Feb. 2004.

[3] Anon., "Space Vehicle Accelerometer Applications," NASA SP-8102, 1972.

[4] Blanchard, R. C., Larman, K. T., and Barrett, M., "The High Resolution Accelerometer Package (HiRAP) Flight Experiment Summary for the First 10 Flights," NASA RP-1267, 1992.

[5] Bishop, R., and Dubois-Matra, O., "Development of a Planetary Entry Model Suitable for Processing Acceleration Measurements," NASA IR01-01, Apr. 2001.

[6] Wawrzyniak, G., and Lisano, M., "Using Inertial Measurements for the Reconstruction of 6-DOF Entry, Descent, and Landing Trajectory and Attitude Profiles," AIAA/AAS Astrodynamics Specialist Conference, American Astronautical Society, Paper 02-164, San Antonio, TX, Jan. 2002.

[7] Willcockson, W., and Johnson, M., "Mars Odyssey Aerobraking: The First Step Toward Autonomous Aerobraking Operations," *Proceedings of 2003 IEEE Aerospace Conference*, Vol. 8, Inst. of Electrical and Electronics Engineers, Piscataway, NJ, 2003, pp. 3503–3510.

[8] Lyons, D. T., Sjogren, W., Johnson, W., Schmitt, D., and McRonald, A., "Aerobraking Magellan," AIAA/AAS Astrodynamics Specialist Conference, American Astronautical Society, Paper 91-420, Durango, CO, Aug. 1991.

[9] Wong, S. K., You, T.-H., Giorgini, J. D., Lim, L., and Chadbourne, P., "Navigating Through the Venus Atmosphere," AIAA/AAS Astrodynamics Specialist Conference, American Astronautical Society, Paper 94-116, Cocoa Beach, FL, Feb. 1994.

[10] Esposito, P., Alwar, V., Demcak, S., Graat, E., Johnston, M., and Mase, R. A., "Mars Global Surveyor: Navigation and Aerobraking at Mars," AIAA/AAS Astrodynamics Specialist Conference, American Astronautical Society, Paper 98-384, Monterey, CA, Feb. 1998.

[11] Smith, J., and Bell, J., "2001 Mars Odyssey Aerobraking," AIAA/AAS Astrodynamics Specialist Conference, AIAA, Paper 2002-4532, Monterey, CA, Aug. 2001.

[12] McRonald, A., "Use of Atmospheric Drag to Circularize an Elliptic Spacecraft Orbit at Venus," Jet Propulsion Lab., California Inst. of Technology Rept. 760-163, Pasadena, CA, 1977.

[13] Mase, R. A., "2001 Mars Odyssey: Navigation Plan and Trajectory Characteristics; Final Version," Jet Propulsion Lab., California Inst. of Technology, Rept. D-16001 722-202, Pasadena, CA, 2001.

[14] Mase, R., Antreasian, P., Bell, J., and Martin-Mur, T., "The Mars Odyssey Navigation Experience," AIAA/AAS Astrodynamics Specialist Conference, AIAA Paper 2002-4530, Monterey, CA, Aug. 2002.

[15] Wie, B., *Space Vehicle Dynamics and Control*, AIAA Education Series, AIAA, Reston, VA, 1998.

[16] Julier, S. J., and Uhlmann, J. K., "A New Extension of the Kalman Filter to Nonlinear Systems," *Proceedings of SPIE—The International Society for Optical Engineering*, Vol. 3068, Society of Photo-Optical Instrumentation Engineers, Bellingham, WA, Apr. 1997, pp. 182–193.

[17] van der Merwe, R., and Wan, E. A., "The Square Root Unscented Kalman Filter for State and Parameter-Estimation," *2001 IEEE International Conference on Acoustics, Speech, and Signal Processing*, Vol. 6, Inst. of Electrical and Electronics Engineers, Piscataway, NJ, May 2001, pp. 3461–3464.

[18] van der Merwe, R., and Wan, E. A., "Sigma-Point Kalman Filters for Integrated Navigation," *Proceedings of the 60th Annual Meeting of the Institute of Navigation*, Inst. of Navigation, Alexandria, VA, June 2004, pp. 641–654.

[19] Tolson, R. H., Keating, G. M., George, B. E., Escalera, P. E., Werner, M. R., Dwyer, A., and Hanna, J., "Application of Data to Mars Odyssey Aerobraking and Atmospheric Modeling," *Journal of Spacecraft and Rockets* (to be published); also AIAA 2002-4533, Aug. 2002.

[20] Cancro, G. J., Tolson, R. H., and Keating, G. M., "Operational Data Reduction Procedure for Determining Density and Vertical Structure of the Martian Upper Atmosphere from Mars Global Surveyor Accelerometer Measurements," NASA CR-1998-208721, 1998.